SAND2022-4288C

ILASS-Americas 32nd Annual Conference on Liquid Atomization and Spray Systems, May 22-25, 2022

A Study of Thermal Characteristics and Fuel Film Evaporation of Fuel Sprays Impinging on a Surface

M. Dhanji*, L. White, T. Nguyen, L. Pickett and J. Manin
Sandia National Laboratories
Combustion Research facility
7011 East Avenue
Livermore, CA 94550 USA

Abstract

Gasoline sprays injected during cold-start and low-load conditions result in the formation of high levels of soot and unburnt hydrocarbons. It is understood that these emissions are originating from piston and wall wetting. Various technological advancements to date have helped mitigate these issues, but there remains a lack of understanding related to the effects of fuel injection on the impinging surfaces' transient thermal characteristics leading to fuel film evaporation rate and pollutant formation. Analysing these aspects can help refine the engine designs further to help reduce tailpipe emissions. In this work, we investigate the effects of fuel injection impinging on a wall from spatially and temporally resolved temperature measurements. The experiments were performed inside a constant-volume chamber, with the sprays impinging on a temperature-controlled wall equipped with nine thermocouples. The facility can reproduce fuel, charge gas and wall temperature conditions relevant to the cold start and warm-up period of gasoline engines. The results capture the dynamic behaviour of the temperature field following initial spray impingement and film formation, enabling temporally-resolved heat flux calculations. Surface cooling was observed when the hot fuel at 353 K impinged on the heated wall (363 K) 40 mm downstream, with the highest reduction in the heat flux magnitude observed in the plume center region. This was due to evaporative cooling as the mixture fraction changed phases. Under the cold chamber conditions, the surface cooling or heating in the plume center was dependant on the ambient density. Increasing the ambient density to 3 kg/m^3 had resulted in surface heating as measured by the probes located in the plume center and wall jet regions. This was due to the high entrainment rate of the fuel upon injection, which resulted in convective heat transfer between the surrounding hot mixture and the vapourising fuel.

*Corresponding Author: mpdhanj@sandia.gov

Introduction

While Gasoline Direct Injection (GDI) engines have become the dominant mode of power-trains for light duty applications, an ongoing challenge associated with GDI engines is achieving a suitable homogeneous-stratified charge for the cold-start or part-load operations. To enable the rapid activation of the exhaust catalyst, one common strategy is to implement a combination of late multiple injections in the compression stroke and late ignition in the expansion stroke within the first few cycles. This increases the ambient temperature of the combustion chamber during cold starts, progressively leading to the transient thermal loading on the chamber's surfaces. This technique, however, is often accompanied by incomplete and unstable combustion [1]. This is due to the complex interactions between the in-cylinder flow and direct fuel injections, along with their impact on the ignition timing and initial flame development.

The uneven distribution of the mixed gases in the cylinder has a direct effect on the emissions levels. A reduction in the lambda value from stoichiometric to 0.9 has been reported to result in an almost threefold increase in the particulate number (PN) [2, 3], which subsequently increases the formation of carbon monoxide (CO) and smoke levels [4].

One way to reduce the PN levels formed under cold-start conditions is to reduce fuel impingement on the chamber's surfaces, which results in diffusion flame combustion. This is especially crucial when the surfaces are relatively cold, which inhibits fuel vaporization. As such, an accelerated warm-up of the piston, controlling the spray's trajectory, enabling a high rate of atomization, reducing the penetration length, and optimizing the spray cone angle all play crucial roles in alleviating the surface impingement and fuel film formation [5, 6]. These requirements can be achieved by employing carefully designed multiple fuel injections within one cycle, which can form temporally and spatially well adjusted fuel and air mixture.

The double injections strategy can help improve the turbulence levels of the flow [7] and avoid a high concentration of liquid spray piling up on the sprays' tips [8]. Kumar et al. [3] noted a reduction in soot levels when employing double injections. This was due to reduced wall wetting and pool fire when tested at engine conditions of 2000 rpm, wide-open throttle conditions, and injection pressure of 20 MPa. An early first injection provided the fuel adequate time to evaporate, producing a favourable homogeneous mixture prior to the second injection.

Raman et al. [4] studied the effects of double injections and spark timings on the catalyst light-off. A two-phase light-off process was recommended. In phase 1, the spark timing should be advanced before top-dead center for the first few cycles of the light-off period. The fuel injection timing can subsequently be adjusted with the spark timing. This is to avoid misfire and enable rapid engine warm-up, reducing the hydrocarbon and CO emissions. Phase 2 consists of multiple injections and retarded spark ignition which increases the exhaust temperature. In this phase, the main focus is to generate high exhaust enthalpy to enable catalyst light off. Throttled stoichiometric operation with double injections strategy can help generate a stratified mixture and improve the combustion stability here.

The timings of the multiple injections are key in controlling the mixture distribution in the cylinder. An early first injection in the compression stroke results in high evaporation rate and improved mixture homogeneity. The fuel in this case has sufficient time to vaporize, disperse and is reported to be guided in a counter-clockwise direction by the tumble flow. This increase in the intensity of the tumble motion enhances the mixture entrainment [9].

With late injections in the compression stroke, high in-cylinder pressure and high turbulent kinetic energy affect the mixture formation and distribution. As such, the influence of the in-cylinder flow and charge density on the spray development should be investigated when considering late injections [10]. Retardation of the second injection close to the top-dead center (TDC) has led to high mixture inhomogeneity [11, 12]. Increasing coefficient of variation of both the indicated mean effective pressure and peak cylinder pressure were observed with delayed second injections, which had consequently increased the cyclic variability as the mixture cloud from the second injections approached TDC. In this case, there was less time for fuel diffusion, resulting in the termination of the combustion, as reported in [1]. As a result of the high mean equivalence ratio near the spark plug, slower and more fluctuated initial flame propagation had occurred, which can be recovered if the local TKE levels are high. Additionally, the multiple injections late in the compression stroke causes heavy piston surface wetting, thereby increasing soot and hydrocarbon emissions.

The injection pressure plays a key role in the atomization rates of the injected fuel and in the mixture formation. Small Sauter mean diameter of the fuel droplets and large spray angles were formed as a result of the high injection pressure, as reported in [13, 14] . As a result, the fuel droplets had spread radially across the cylinder, improving the mixing

of the air and fuel. This helped in achieving a well-mixed homogeneous charge. Although the main tip penetration length increased with increasing fuel injection pressure, the critical spray breakup had occurred closer to the injector tip.

In a previous study on the injection pressures ranging between 5 MPa and 40 MPa using a multi-hole injector [15], it was observed that the PN levels decreased with increasing injection pressure. The reasons for this were twofold: the enhanced atomization rate and air entrainment from high injection pressure improved the mixture homogeneity; and the coking deposit accumulation and diffusion combustion had been alleviated, which was also reported in [16][17].

Few studies have investigated the heat transfer effects on chamber surfaces during cold starts. Yang et al. [18] performed three-dimensonal simulations of the transient engine flow, spray and combustion over the first three consecutive engine cycles. This was to enable accurate predictions of the in-cylinder flow dynamics and transient wall temperatures during cold starts. They implemented engine speed and 1D conjugate heat transfer model, and used measured data obtained from a production four-cylinder spark-ignition direct-ignition engine for validation. A 6-hole injector with a plume angle of 16.7° was used, with fuel pressure of 10 MPa. The combustion chamber's surface was observed to have a temperature rise of 2 K per cycle, which is reported to have limited effect on the mixing and combustion processes in the first 3 cycles. The wall surface temperature varied with the stroke, piston motion and the combustion process, while the increase in the piston surface temperature was found to be greater than that of the cylinder head and liner.

Spatio-temporally resolved measurements of the liquid fuel-film thickness after fuel impingement were obtained using UV absorption imaging [19]. The measurements were performed using an 8-hole "Spray G" injector from Engine Combustion Network (ECN) inside a constant volume chamber, with a transparent plate mounted 30 mm from the nozzle perpendicular to the injector axis. Here the ambient pressure and temperature were 0.1 MPa and 100 °C respectively, with an injection pressure of 20 MPa and fuel temperature of 100 °C. The measurements revealed that the evaporation rate was more prominent at the upstream, inward edges of the fuel films, where the film thickness was smaller than that measured downstream at the outer edges of the spray. The fuel mass had decreased by 68% between 4 ms to 20 ms aSOI. Of the total fuel impinged on the wall 30 mm downstream, 7% of the initial fuel mass was reported to have remained on the plate 30 ms aSOI.

Schulz et al. [20], performed infrared thermography to study the fuel deposits on the walls of a combustion chamber using a heated Nickel alloy plate to substitute the piston surface. They analysed the heat transfer effects of plume impingement by varying four features: the impact angle of the spray jet, the axial distance between the injector and the heated plate to 15 mm, 25 mm and 50 mm, the wall temperature, and the injection pressure which was set to 5 MPa, 15 MPa and 30 MPa. A decrease in the wall surface temperature at the spray impingement zone was measured. A high injection pressure and plume's impact angle adjustment were recommended in order to reduce the mass of film accumulated on the wall. Increasing the injection pressure had raised the heat flux to the maximum and had resulted in a reduction in the wall film mass. With increasing axial distance between the nozzle and the wall, the wall heat flux had decreased, which was a consequence of increased impact area. The study however, was not able to identify the initial temperature of the fuel deposited on the wall using this technique.

The aim of the current study is to therefore investigate the effects of fuel impingement on the spatial and temporal temperature variations and the heat flux characteristics of the surface of the wall under different ambient conditions representing hot chamber surfaces and cold-starts. The subsequent part of the article describes the test setup and specifications of the hardware used to perform the measurements, along with an overview of the test matrix. This section is then followed by results and discussions whereby three different conditions are investigated. Key conclusions and an overview of future works are presented in the final part of the article.

Methodology

Fuel was injected into Sandia's optically accessible high pressure and high-temperature combustion vessel. The test injector used was a solenoid activated, 8-hole ECN "Spray G" injector by Delphi [21]. The key focus was to study the impact of a single plume of the spray G injector on the surface of the wall. In this case, the fundamentals of the free spray, as presented in Figure 1, provides an overview of the key mechanisms and features of the spray upon impingement. The schematic shows the fuel film formation upon impact along the free spray plume direction. As the majority of the liquid film settles on the surface, the low mixture fraction behind the head of the free spray, labelled the 'main wall jet region', propagates parallel to the wall. The wall jet progressively experiences increasing resistance from the surrounding gases, enabling the formation of wall jet vortices around the edges of the film centre region and the main wall jet region.

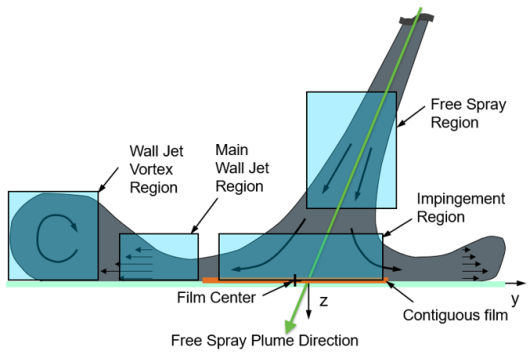

Figure 1. A conceptual model of a single plume impinging on a solid surface. The schematic provides indication of the fuel film settling on the surface upon impingement, and a portion of the mixture fraction moving parallel to the wall in various directions, generating a wall jet and subsequently a wall jet vortex as it experiences increasing drag caused by the ambient gases.

The injector's orifice drill angle is 37° relative to the nozzle axis. It is worth noting however, that the plume direction may not be the same as the drill angle due to the complexities associated with the internal nozzle flow as well as the plume to plume variations. The injector was operated at 20 MPa, and the fuel mix used was 30% toluene and 70% isooctane by volume. This fuel mix was used due to a parallel study performed on film thickness quantification using optical diagnostics [19] which required a tracer concentration in order to capture the signal. A double injection strategy was employed, with the electronic injection duration of 0.78 ms and dwell time of 1 ms. The injected mass was 10.3 mg per injection, resulting in total injection mass of 20.6 mg as a result of the double injection strategy.

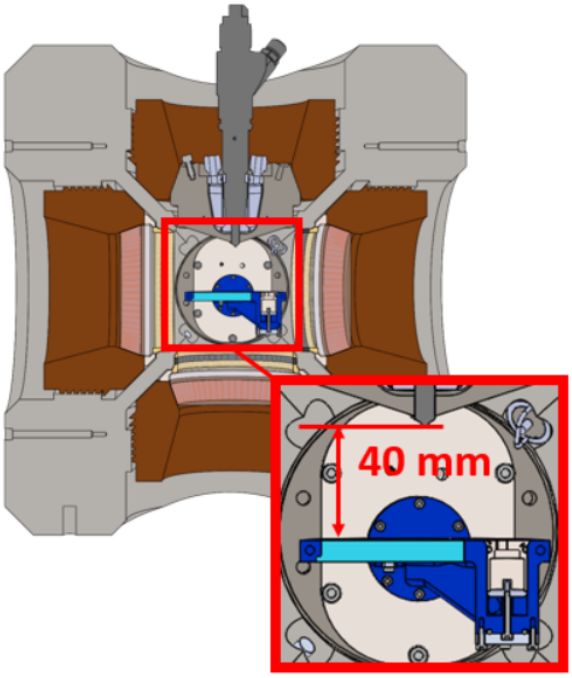

Figure 2. A schematic of the spray chamber showing the temperature controlled wall placed 40 ms downstream of the injector tip.

A temperature controlled wall was placed 40 mm away from the injector's tip as shown in Figure 2. This setup is representative of the piston's axial distance from the injector tip in the compression stroke undergoing multiple injections during cold starts. The wall's design is shown in Figure 3. The injector was configured to have one of the 8 plumes impinging directly onto the thermocouples.

The probe housed nine fast response, thin surface, K-Type coaxial NiCr-Ni thermocouples, mounted in the orientation shown in Figure 3. The thermocouples' design details and further specifications are reported in [22]. These thermocouples possess high thermal and mechanical resistance, along with high signal-to-noise ratio. The resolution of each thermocouple was 40 µV/K. The high temporal resolution required the thermocouples to have response time in the range of a few microseconds. To achieve such high resolution, the layer of coating with small thickness is required, with less than 2 µm

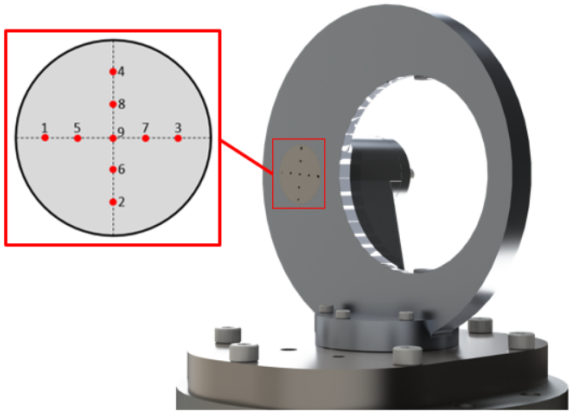

Figure 3. The design of the temperature controlled wall with the thermocouples mounted and numbered in the orientation shown. The wall also housed a fused silica window which was used for optical diagnostics as a separate campaign.

at the surface of the thermocouple junction. To accommodate this requirement, a Cr and Au coating of 0.3 µm was applied. These nine thermocouples were installed inside a housing made of aluminium alloy. The telemetry system consisted of the 9 thermocouples, K type thermocouple conditioner AD595, and 5000 series Picoscope where the measured voltages were sampled at 6 MHz.

The top image in Figure 4 shows the probes' positioning with respect to the plume's impingement location and the plume direction for measurements of the hot chamber conditions after the second injection. The bottom image on the other hand, shows the probes' positions with respected to the plume's location for the cold chamber conditions after the second injection. These images are obtained from parallel optical diagnostics (Laser Induced Fluorescence), imaged through the fused silica window. As the thermocouple probes' housing was not optical, the authors used their knowledge of the the 8 plumes' orientation with respect to each other 40 mm downstream and rotated the plume that impinged on the window to overlay it on the thermocouples. This was done to provide a representation of the plume targeted directly on the thermocouples. This was for visualisation purposes so that the transient temperature trend can be analysed with respect to the plume centre, the wall jet and plume's tail regions. As these images were obtained from the camera looking through the fused silica window, the rotated plume in that viewing direction resulted in the vertical probe locations shown (probes 4, 8, 6 and 2) being inverted from the design position (Figure 3).

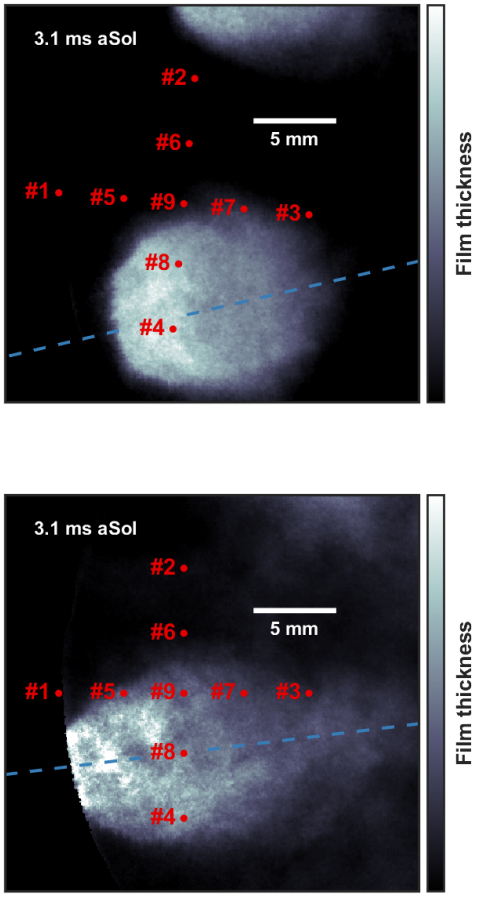

Figure 4. Probes' locations with respect to the plume's footprint and its direction of travel (dashed line across the image). The top image represents plume impingement after second injection for the hot chamber conditions.The bottom image represents impingement after the second injection for the cold chamber conditions.

A cooling circulation pathway inside the wall enabled the coolant to circulate around the wall, which allowed control of the wall temperature. In this case, the wall could be cooled to a desired temperature to simulate cold chamber surfaces during cold-starts. To ensure that the thermocouple probe and the corresponding cables were operative under high ambient pressure with the coolant circulation enabled, the probe and the cables were pressure sealed, with the cables further sealed in an umbilical cord.

The three test cases studied are listed in Ta-

Case	T_{amb}	T_{fuel}	T_{wall}	ρ_{amb}
1	363 K	353 K	363 K	1 kg/m^3
2	363 K	299 K	293 K	1 kg/m^3
3	363 K	299 K	293 K	3 kg/m^3

Table 1. Overview of the test cases. T_{amb}, T_{fuel}, and T_{wall} represent ambient, fuel and wall temperature, respectively. ρ_{amb} represents the ambient chamber density.

ble 1. Here ρ_{amb} represents the ambient density of the chamber. Case 1 represents the hot chamber conditions, where the spray dynamics and fuel film evaporation rate were studied. Case 2 and 3 simulate the cold start with hot ambient chamber conditions. The variations in densities are used to understand the effects of varying load conditions on the free spray jet, entrainment rate and the fuel film's characteristics .

The chosen sampling rate and the telemetry configuration resulted in the high frequency noise being measured along with the temperature trends, as seen in Figure 5. In order to attenuate the noise without compromising the detected temperature variations, a low pass filter was applied, with an cut-off frequency of 8 kHz. This led to some noise still being present in the trends, affecting the heat flux calculations. To resolve this further, a moving average of 100 samples per window was applied to the filtered temperature traces. This not only helped resolve the heat flux magnitudes, but it also helped in distinguishing small differences in the measured temperature trends.

Three repetitions were obtained for each test case, from which the average temperature trend was measured. Due to the low sample number of the repetitions, instead of reporting the uncertainties associated with the averaged data, the average results are plotted along with individual measurements to provide an indication of the agreement between averaged traces and the individual test cases. In order to better interpret the temperature variations measured using each probe, we report the the temporal trends of the temperature difference $\delta T = T_0 - T_i$.

Cook-Felderman's technique [23] was used to calculate the wall heat flux (1). The classic heat transfer solutions for a 1-D semi-infinite body, including the Fourier series for heat flux calculation, require the domain to initially be at a constant, uniform temperature. The current application does not have a uniform wall temperature, but instead consists of a startup transient whereby a steady-state

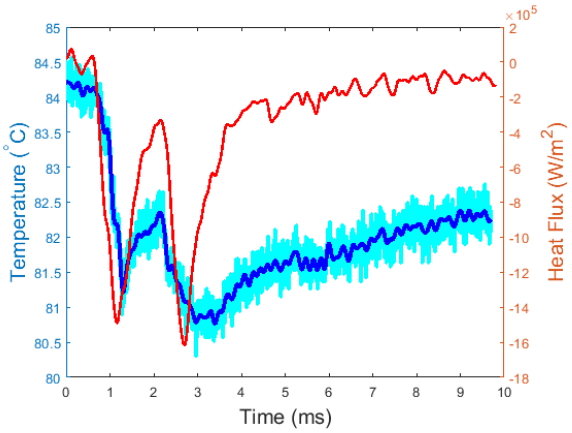

Figure 5. Raw and filtered temperature traces measured by probe No. 8 indicating the variations in the filtered temperature as a result of applying a low pass filter with an attenuation frequency of 8 kHz. The corresponding heat flux trend is presented on the right-hand side axis. The associated chamber conditions are $T_{amb} = 363\,\text{K}$, $T_{wall} = 363\,\text{K}$, $T_{fuel} = 353\,\text{K}$ and $\rho_{amb} = 1\,\text{kg/m}^3$.

wall profile is established [24].

$$q"_{\omega}(t) = \frac{2b}{\sqrt{\pi}} \sum_{n=1}^{N} \frac{T_j - T_{j-1}}{\sqrt{t_n - t_j} + \sqrt{t_n - t_{j-1}}} \qquad (1)$$

The Cook-Felderman technique eliminates the requirement of the uniform initial condition of the wall. The technique uses a truncated summations series to numerically calculate the surface heat flux. In this case, b denotes the temperature dependant thermal effusivity ($b = \sqrt{\lambda \rho c_p}$). The correct use of the thermal effusivity for the heat flux calculation is described in [22]. In summary, the thermal effusivity should be determined for specific pairing of materials. Emmrich [25] used a polynomial function to calculate the thermal effusivity of an aluminium alloy piston. The thermal properties used were reported to match that of the pairing used in the current work. As such, the temperature dependant thermal effusivity used to calculate heat flux has been determined from their measured relationship between temperature and thermal effusivity. The right-hand side axis presented in Figure 5 shows the heat flux trend corresponding to the filtered temperature trend.

Results and Discussions

1 Hot Chamber Conditions

This section discusses the temperature differences, after injection of a double injection strategy, for the hot chamber conditions whereby T_{amb} = 363 K, T_{fuel} = 353 K, and T_{wall} = 363 K. Figure 6 shows the transient change in temperature as recorded by the thermocouples. The trends show that the initial δT is zero, until the plume arrives 0.6 ms after the start of first injection. Upon the arrival of the plume, a transient reduction in the surface temperature is observed, measured by all the thermocouples. This occurs in spite of the fuel being heated to 353 K. The greatest cooling is observed by probe No. 8, located in the plume center region (top image in Figure 4) while probe No. 3, located in the plume's tail region, shows the least change in temperature.

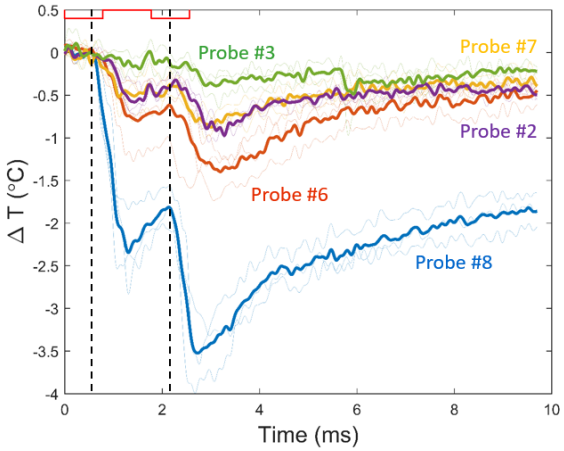

Figure 6. Transient change in temperature after fuel impingement from a double injection strategy measured using five thermocouples in the orientation presented in the top image of Figure 4. The chamber conditions are: T_{amb} = 363 K, T_{wall} = 363 K, T_{fuel} = 353 K and ρ_{amb} = 1 kg/m^3. The red trends at the top of the plot represent the double injection timings. The vertical dashed lines indicate the plume center's arrival on the wall, which are 0.6 ms aSOI-1 and 0.3 ms aSOI-2.

After the first fuel impingement, the temperature is observed to increase as a consequence of the high thermal mass of the wall and progressive fuel film vaporization. The rise in temperature is interrupted by the impingement of the second injection. This time, the impact of the second injection occurs earlier (0.3 ms after start of second injection), when compared to the impact timing of the first injection.

The heat flux trend presented in Figure 7 shows that the magnitude of the heat flux after each injections are generally comparable, but the second injection shows a slightly greater reduction in the heat flux compared to the first injection, as consistently measured by all the five thermocouples. This occurs because of the low thermal inertia of the wall, whereby the heat flux does not return to zero prior to the start of the injection. This indicates that the wall is cooled by the first injection. As such, the mixture fraction from the second injection impinging on the wall's surface results in further cooling of the wall. This effect is more predominant with the probes located in plume center region and less noticeable in the wall jet region.

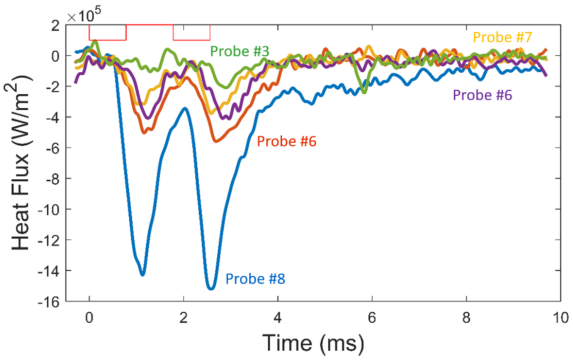

Figure 7. Heat flux calculated using the Cook-Felderman technique for the hot chamber conditions.

The probes located in the wall jet region show δT returning to zero by 10 ms. This is not the case for the plume center region (probe No. 8). Shway et al. [19] noted a 68% reduction in the fuel mass between 4 ms to 20 ms aSOI. The current trend in the plume center region indicates the presence of the fuel film up to 10 ms aSOI.

Figure 8 shows the relationship between the adiabatic mixture fraction of the fuel and its corresponding temperature at the equilibrium state. The equilibrium-state calculations are performed to predict liquid and vapor fraction for different mixtures. These predictions are calculated using standard energy and fugacity balance equations for liquid fuel and gas, which are set to initial set-point temperatures during the experiments. The calculations predict mixture composition and temperature at the equilibrium state. The solid black line in figure 8 represents the changing liquid/vapor mixture under complete and incomplete evaporation conditions. Here a mixture fraction of 1 indicates perfect liquid at the injection temperature of 353 K. The black

dashed line represents the fuel having transitioned to a fully vapour phase, whose temperature increases to match that of the chamber temperature as a result of convective heat transfer between the ambient hot gases and the fuel vapour. The transition region between both these regions is a saturated vapor-liquid equilibrium mixture. This means that no liquid will exist below the mixture fraction lower than the saturated vapor-liquid equilibrium mixture, given that the fuel vapourisation is driven entirely by the mixing process and perfect equilibrium mixtures are formed.

The trend presented here indicates that as the mixture fraction of the fuel reduces, the fuel undergoes evaporative cooling as a result of heat absorption due to the phase change. This energy transfer causes the fuel to cool, and at the point of impact 40 mm downstream, the cooled fuel mixture subsequently causes conductive cooling on the wall's surface, as observed in Figure 6.

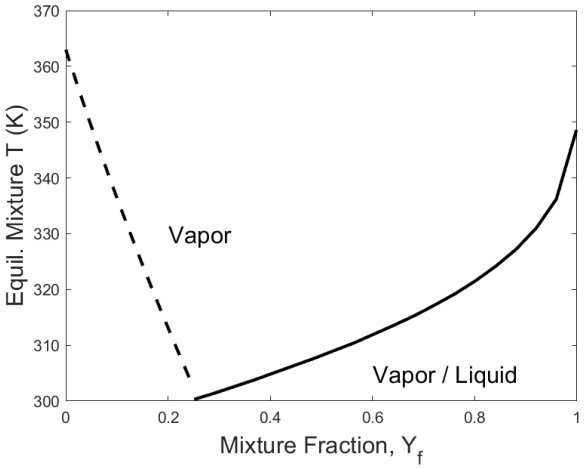

Figure 8. The relationship between adiabatic mixture fraction and the equilibrium temperature for the hot chamber conditions. Solid black line represents the mixture containing liquid and vapour mixture, while the black dashed line represents the fuel having transitioned to a fully vapour phase.

The plume center possesses a mixture fraction of 0.35, 40 mm downstream of the injector, as determined using the Musculus-Kattke model. The equilibrium temperature for this mixture fraction is 303 K, 50 K lower than the fuel injection temperature. This results in the wall cooling of 3 K in the plume center region (blue line in Figure 6) upon the mixture's impingement on the wall.

Furthermore, while the extent of cooling in the plume's centre region is the greatest, the extent of cooling measured by the probes located in the wall jet of the free spray (Figure 1) is relatively low. The wall jet region and the wall jet vortices formed upon fuel impingement would likely possess mostly vapourised mixture. This is the point at which the vapour would be undergoing convective heat transfer from the surrounding hot gases. As a result of the reduced temperature difference between the wall temperature and the wall jet's (equilibrium) temperature, the extent of cooling is lower than that observed in the plume center region.

Probe No. 6 is located parallel to the plume centre region, which experiences greater extent of wall cooling as opposed to the probes located along the plume's edges (probe No. 5 and No. 7). Probe No. 6 experiences greater cooling compared to the other probes located in the wall jet region potentially due to the direction of the wall jet's travel, as well as the greater likelihood of the wall jet vortices between the two adjacent plumes interacting in this region.

2 Cold Chamber Conditions, Low Ambient Density

This section discusses the temperature differences for the cold chamber, with hot ambient conditions whereby $T_{\text{amb}} = 363\,\text{K}$, $T_{\text{wall}} = 293\,\text{K}$, $T_{\text{fuel}} = 299\,\text{K}$ and $\rho_{\text{amb}} = 1\,\text{kg/m}^3$. Figure 9 shows the transient change in temperature as recorded by the nine thermocouples. The trends recorded in this case indicate surface heating upon fuel impingement. The fuel arrival times after both injections match those reported for the hot chamber conditions, indicating that the arrival time is not significantly affected by the chamber temperature.

It can be noted that upon impact of the first injection, majority of the probes measured an increase in the surface temperature, with the exception of the probes located in the plume center region. To better represent the transient δT measured by each probe with respect to the plume's position and its direction of travel, Figure 10 shows the scattered (linear) interpolant plots of δT for various time instances after start of injection. The red bullets indicate the thermocouple positions. The overlaid plume in the plots originates from LVF contours obtained through Computer Tomography measurements 40 mm downstream, reported in [26].

The plot at 1.5 ms aSOI-1 indicates a significant rise in temperature by the probes located in the wall jet region, along the direction of the plume. Meanwhile, the probes in the plume's center and tail regions indicate negligible heat transfer effect upon fuel arrival. This indicates that the low mixture fraction in the wall jet region causes the greatest heat

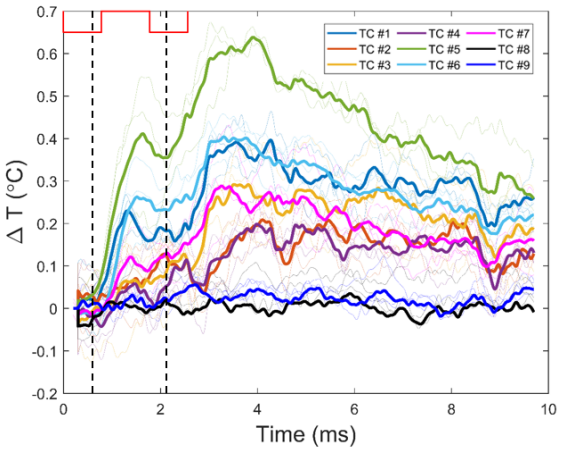

Figure 9. Transient change in temperature after fuel injection from a double injection strategy, measured using nine thermocouples. The test conditions are: $T_{\text{amb}} = 363\,\text{K}$, $T_{\text{wall}} = 293\,\text{K}$, $T_{\text{fuel}} = 299\,\text{K}$ and $\rho_{\text{amb}} = 1\,\text{kg/m}^3$. The vertical dashed lines represent the plume center's arrival on the wall, which are 0.6 ms aSOI-1 and 0.3 ms aSOI-2.

transfer from the free spray to the wall's surface. The second injection at 3.1 ms (or 1.3 ms aSOI-2) still results in the greatest rise in temperature in the wall jet region, but this time we observe conductive heating in the plume's tail region. At 2.2 ms aSOI-2, the tail region sees a reduction in the wall heating, while the probe located in front of the plume in the plume's direction, remain heated. In all this, the heavily wetted region, which is the plume's center region, indicates no net heat transfer from the fuel to the wall.

The plot in Figure 11 shows the trend of the average mixture fraction along a plume's radial location. These plots indicate peak LVF located in the plume's center region, indicating heavy surface surface wetting, which exhibits no heat transfer effects upon the plume center's impact. The mixture fraction under these conditions, as predicted by the Musculus-Kattke model, is approximately 0.3 . Figure 12 shows the relationship between the adiabatic mixture fraction of the fuel and its corresponding equilibrium temperature.

The trend for the $1\,\text{kg/m}^3$ ambient density indicates that as the mixture fraction decreases, the fuel is undergoing evaporative cooling, before fully vaporising and undergoing convective heating from the surrounding hot ambient fluid. It can be observed that the overall change in temperature as the mixture fraction reduces under the vapor/liquid phase is 3 K. This change is small. For the mixture fraction of 0.3, 40 mm downstream, the temperature of the fuel is 294 K. Since the wall is cooled to 293 K, the temperatures of both the impinging fuel and the surface of the wall are comparable. This is why the plume centre region experiences negligible effects of heat transfer as the fuel impacts the wall.

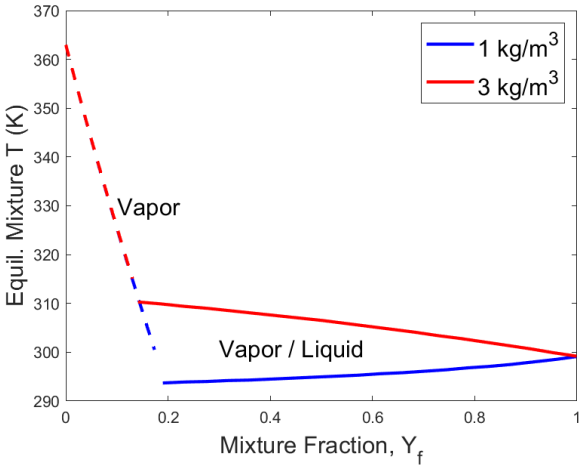

Figure 12. The relationship between adiabatic mixture fraction and the equilibrium temperature for the cold chamber conditions. The solid lines represent the mixture containing liquid and vapour mixture, while the dashed lines represent the the fuel having transitioned to a fully vapour phase.

The vaporised mixture undergoes heating until the temperature matches that of the ambient temperature during complete vaporisation. The rise in temperature measured by the probes located along the wall jet is therefore the result of the high vapour concentration fuel here undergoing convective heat transfer with the ambient gases. This effect is more pronounced after the second injection compared to the first injection.

3 Cold Chamber Conditions, High Ambient Density

The temperature differences for the cold chamber, with hot ambient conditions whereby $T_{\text{amb}} = 363\,\text{K}$, $T_{\text{fuel}} = 299\,\text{K}$, $T_{\text{wall}} = 293\,\text{K}$ and $\rho_{\text{amb}} = 3\,\text{kg/m}^3$ are discussed in this section. Figure 13 shows the transient change in temperature as recorded by the thermocouples. The surface heating under the higher ambient density is observed to greater when compared to the lower ambient density. In this case, the probes located in the plume centre region (probe Nos. 8 and 9) also show an increase in temperature after both injections' impact on the

wall's surface.

Furthermore, the higher ambient density is observed to delay the fuel arrival time caused by increased entrainment rates of the fuel mixture. The arrival is delayed to 1.1 ms after the start of first injection, while the second injection's arrival time is delayed by 0.6 ms after start of second injection.

Figure 14 shows the scattered interpolant plots of δT for various time instances after start of injection. The plots show that the plume center region experiences increase in temperature comparable to the probes located in the wall jet region at 1.7 ms. At this time, the plume's tail region experiences no heat transfer effects upon impact. This region can be observed to progressively heat up, especially after the second injection (the plot shown at 2.4 ms). This is again indicative of conductive heat transfer from the heated plume center and wall jet region, to the plume's tail region, which is accelerated by the impact of the second injection.

As the fuel travels 40 mm downstream, the mixture fraction in the plume's center is calculated to be 0.23 using the Musculus-kattke model. Observing the temperature trend of the adiabatic mixture fraction (Figure 12) for the ambient density of $3\,\mathrm{kg/m^3}$, instead of evaporative cooling, we observe an increase in temperature as the mixture fraction decreases. This is caused by the high ambient density, which would increase the rate of droplets' entrainment upon injection. As a consequence of higher entrainment rate, the predicted liquid length decreases [27] and the measured plume arrival time observed by the time at which the temperature starts to rise for all the probes, is delayed for the higher ambient density case.

As a result, these droplets would be undergoing phase change faster and experiencing convective heat transfer at a high rate between the hot gases and the fuel mixture fraction. The temperature of the mixture fraction of 0.23 is calculated to be 311 K. The plume center at the time of impingement contains low mixture fraction at high temperature, which upon fuel impingement, results in conductive heat transfer from the plume centre region to the wall's surface.

Conclusions

The current work investigated the heat transfer effects of a fuel spray impinging on a wall under varying chamber conditions. The study was carried out using a series of thermocouples installed on the surface of the wall placed 40 mm away from the injector. One plume of an 8-hole ECN spray G injector was designed to impinge on the thermocouples. This enabled spatial and temporal characterisation of temperature variations upon the fuel's impact on the surface of the wall. A double injection strategy was investigated with hot ambient chamber conditions of 363 K. Three different cases were analysed which represented hot chamber conditions at ambient density of $1\,\mathrm{kg/m^3}$ and cold starts where the surfaces were cooled under two difference ambient densities.

Under the hot chamber conditions, the heated fuel experienced evaporative cooling upon injection due to the heat absorption effects during the phase changes of the free spray. Upon impingement 40 mm away from the injector, the fuel contained low mixture fraction, comparable to saturated vapor-liquid equilibrium mixture. The low equilibrium temperature of the mixture resulting from evaporative cooling led to surface cooling upon impingement. The plume center region resulted in the greatest wall cooling.

Under the cold chamber conditions, conductive cooling or heating of the wall upon fuel impingement was dependent on the ambient density. For the low ambient density of $1\,\mathrm{kg/m^3}$, the equilibrium temperature decreased due to evaporative cooling as the phase of the fuel changed from liquid to vapor/liquid mixture. Under higher ambient density of $3\,\mathrm{kg/m^3}$ of on the other hand, the equilibrium temperature increased as the mixture fraction decreased. This was due to the increased entrainment effects which resulted in convective heat transfer between the hot chamber gases and the low mixture fraction of fuel 40 mm downstream. This subsequently resulted in the conductive heating of the wall, both in the plume centre and the wall jet region.

The upcoming works will focus on the effects of the combustion processes on the wall heat transfer. Investigations will be carried out by applying the existing understanding of the effects of the fuel film impingement and its heat transfer effects at varying chamber conditions, to investigate the effects of the flame generation, arrival time, residence time and soot generation on the measured temperature and heat flux traces.

Acknowledgements

The authors would like to thank Aaron Czeszynski for his assistance with the experimental setup, and for designing and setting up the temperature controlled wall and its mount. Sandia National Laboratories is a multi-mission laboratory managed and operated by National Technology and Engineering Solutions of Sandia, LLC., a wholly owned subsidiary of Honeywell International, Inc., for the

U.S. Department of Energy's National Nuclear Security Administration under contract DE-NA0003525. This paper describes objective technical results and analysis. Any subjective views or opinions that might be expressed in the paper do not necessarily represent the views of the U.S. Department of Energy or the United States Government.

References

[1] Koshiro Kimura, Sachio Mori, Masato Kawauchi, and Rio Shimizu. *International Journal of Engine Research*, 20(4):470–479, 2019.

[2] Frank Dorscheidt, Stefan Sterlepper, Michael Görgen, Martin Nijs, Johannes Claßen, Surya Kiran Yadla, Robert Maurer, Stefan Pischinger, Sascha Krysmon, and Abdelrahman Abdelkader. 1:1–11, 2020.

[3] Rahul Kumar and J. M. Mallikarjuna. *SAE Technical Papers*, (April):1–13, 2020.

[4] Vallinayagam Raman, Yoann Viollet, and Junseok Chang. *SAE Technical Papers*, (April):1–13, 2020.

[5] *SAE Technical Paper 970627*, pp. 1–44, 1997.

[6] Bradford A. Bruno, Domenic A. Santavicca, and James V. Zello. *SAE Technical Paper Series 2003-01-3163*, 2003.

[7] B.E. Milton, M. Behnia, and D. Ellerman. *International Journal of Heat and Fluid Flow*, 22:350–357, 2001.

[8] T. Li, M. Yamakawa, D. Takaki, K. Nishida, Y. Zhang, and H. Hiroyasu. *SAE Technical Papers*, (724), 2003.

[9] *International Journal of Heat and Fluid Flow*, 56, 2015.

[10] Christopher Geschwindner, Patrick Kranz, Cooper Welch, Marius Schmidt, Benjamin Böhm, Sebastian A. Kaiser, and Joaquin De la Morena. *International Journal of Engine Research*, 21(1):169–184, 2019.

[11] M. Costa, U. Sorge, S. Merola, A. Irimescu, M. La Villetta, and V. Rocco. *Energy*, 117:405–415, 2016.

[12] Xinyan Wang, Jun Ma, and Hua Zhao. *International Journal of Engine Research*, pp. 1–14, 2017.

[13] Sanghoon Lee, Yunjung Oh, and Sungwook Park. *Proceedings of the Institution of Mechanical Engineers, Part D: Journal of Automobile Engineering*, 227(7):951–965, 2013.

[14] Bastian Lehnert, Chris Conrad, and Michael Wensing. *SAE Technical Paper Series*, 1:1–11, 2020.

[15] Walter F. Piock, Bizhan Befrui, Axel Berndorfer, and Guy Hoffmann. *SAE Int. J. Engines 2015-01-0746*, 8(2), 2015.

[16] N. Mitroglou, J. M. Nouri, Y. Yan, M. Gavaises, and C. Arcoumanis. *SAE Technical Paper Series 2007-01-1417*, 2007.

[17] Ch Schwarz, E Schünemann, B Durst, J Fischer, and A Witt. *SAE Technical Paper Series*, 01(724), 2016.

[18] Xiaofeng Yang, Tang-Wei Kuo, Kulwinder Sngh, Rafat Hattar, and Yangbing Zeng. *ICEF2017-3630*, pp. 1–8, 2017.

[19] Kamal Shway, Michele Bardi, Gilles Bruneaux, and Sebastian A Kaiser. *ICLASS 2021, 15th Triennial International Conference on Liquid Atomization and Spray Systems, Edinburgh, UK, 29 Aug. - 2 Sept. 2021*, 2021.

[20] Florian Schulz, Jürgen Schmidt, Andreas Kufferath, and Wolfgang Samenfink. *SAE International Journal of Engines*, 7(3):1165–1177, 2014.

[21] 2021 National Technology and LLC (NTESS) Engineering Solutions of Sandia. *Engine Combustion network (https://ecn.sandia.gov/)*.

[22] Daniel Mayer, Alexander Seelig, Torsten Kunz, Fabian Kopple, Matthias Mansbart, and Michael Bargende. *SAE Technical Papers 2018-01-1782*, pp. 1–18, 2018.

[23] W. J. Cook. *AIAA Journal*, 8(7):1366–1368, 1970.

[24] Terry Hendricks and Jaal Ghandhi. *SAE International 2012-01-1208*, 5(3):1268–1285, 2012.

[25] T Emmrich. PhD thesis, University of Stuttgart, 2010.

[26] Lukas Weiss, Michael Wensing, Joonsik Hwang, Lyle M. Pickett, and Scott A. Skeen. *Experiments in Fluids*, 61(2):1–17, 2020.

[27] Dennis L. Siebers. *SAE Technical Papers*, (724), 1999.

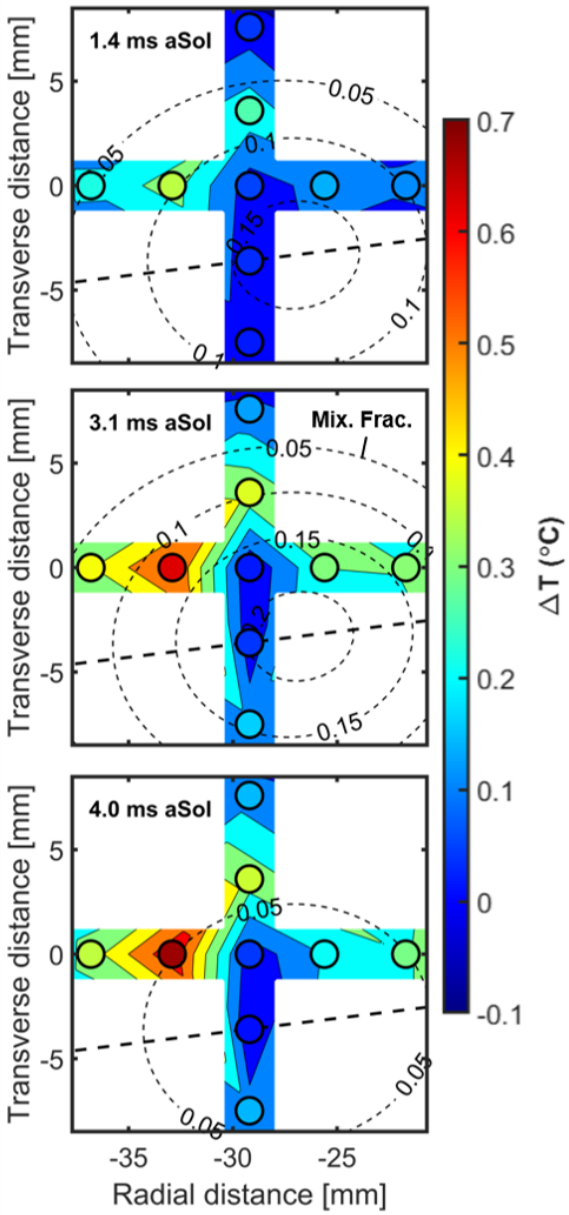

Figure 10. Scattered interpolant plots indicating the temperature distribution measured by the nine thermocouples with respect to the plume centre region and its direction of travel. The test conditions are: $T_{\text{amb}} = 363\,\text{K}$, $T_{\text{wall}} = 293\,\text{K}$, $T_{\text{fuel}} = 299\,\text{K}$ and $\rho_{\text{amb}} = 1\,\text{kg/m}^3$. The overlaid labelled contour of the plume in the plots originate from the Musculus-Kattke mixture fraction.

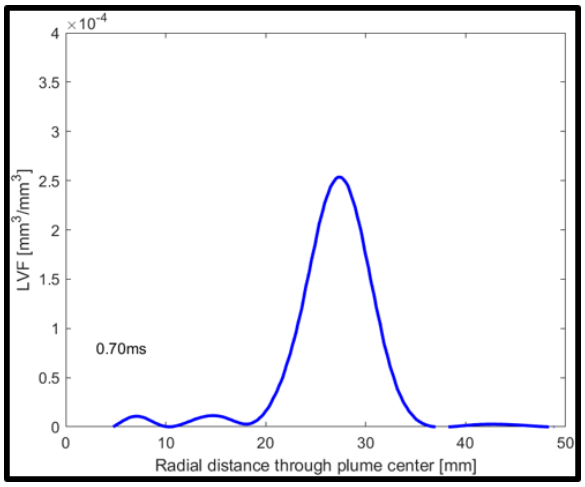

Figure 11. Tomographically reconstructed spray and its liquid-volume fraction in the 'XY' plane, 40 mm downstream from the injector for ECN G3 cold conditions with the ambient density of $1\,\text{kg/m}^3$. The plot shows the LVF (averaged over 8 plume) across the radial locations of a single plume [26].

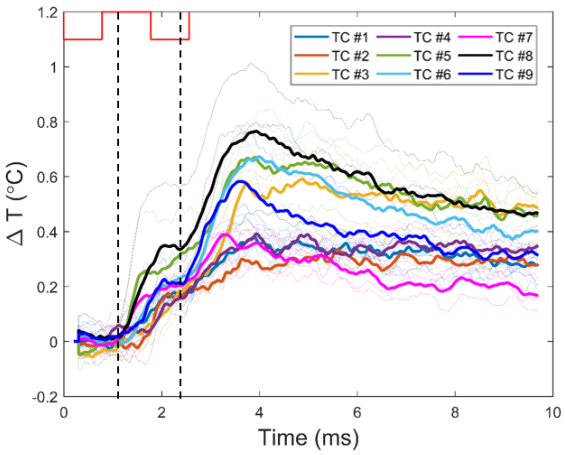

Figure 13. Transient change in temperature after fuel injection from a double injection strategy, measured using nine thermocouples. The test conditions are: $T_{\text{amb}} = 363\,\text{K}$, $T_{\text{wall}} = 293\,\text{K}$, $T_{\text{fuel}} = 299\,\text{K}$ and $\rho_{\text{amb}} = 3\,\text{kg/m}^3$. The vertical dashed lines represent the plume center's arrival on the wall, which are 1.1 ms aSOI-1 and 0.7 mm aSOI-2.

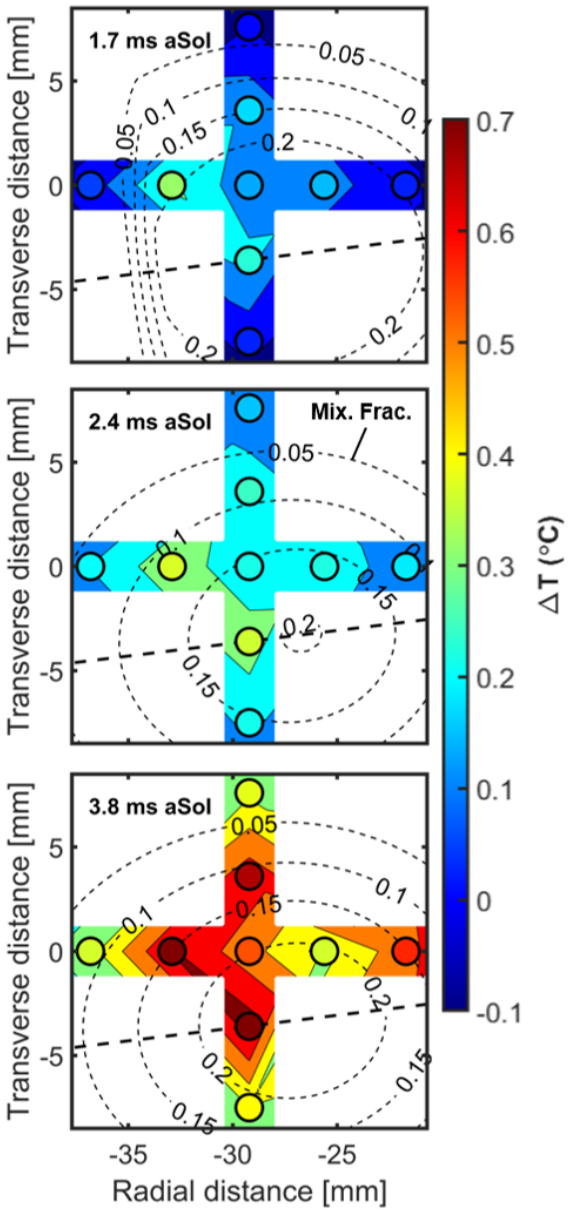

Figure 14. Scattered interpolant plots indicating the temperature distribution measured by the nine thermocouples with respect to the plume centre region and its direction of travel. The test conditions are: $T_{\text{amb}} = 363\,\text{K}$, $T_{\text{wall}} = 293\,\text{K}$, $T_{\text{fuel}} = 299\,\text{K}$ and $\rho_{\text{amb}} = 3\,\text{kg/m}^3$.The overlaid labelled contour of the plume in the plots originate from the Musculus-Kattke mixture fraction.